(Received 7 August 2025, Accepted 7 October 2025, Scheduled 18 October 2025)

Calculation of Equivalent Series Resistance of an Annular Receiving Coil with an Embedded Magnetic Core

Ruichen Qian[1,2], Chenzhi Lu[1,2], Zhixin Li[1,2,], Xinyu Li[1,2,], Kewei Zhu[1,2,], and Jinyang Gao[1,2,*]

[1]*Key Laboratory of Extreme Environment Optoelectronic Dynamic Measurement Technology and Instrument North University of China, Taiyuan 030051, China*
[2]*Key Laboratory of Micro/nano Devices and Systems, Ministry of Education, North University of China, Taiyuan 030051, China*

ABSTRACT: The annular micro receiving coil (RC) holds promise in the wireless power supply for capsule endoscopy (CE). The equivalent series resistance (R_{SR}) of the RC plays a critical role in energy transmission efficiency. Calculating R_{SR} is challenging because RC typically incorporates an embedded magnetic core. To overcome this challenge, this paper employs Dowell's method and Bessel's method respectively to calculate R_{SR}. The analyzed RC consists of an annular core with two grooves and dual windings positioned within the grooves. The influence of the magnetic core on the R_{SR} is equivalently considered through the winding skin effect and core losses. We compared the simulated, calculated, and measured values of the R_{SR}, and found that the error of Dowell's method becomes smaller when the groove spacing $(D_g) > 4$ mm, but fails to capture the influence of D_g on the R_{SR}. Conversely, Bessel's method effectively captures the influence of D_g but exhibits larger errors ($2.09\% \sim 26.52\%$). Based on this finding, we propose a novel Bessel-modified Dowell's (BMD) method by integrating the framework of Dowell's method with a proximity-effect correction term from Bessel's method, which reduces the maximum calculation error to within 13.72%, facilitating rapid optimization of annular coils with embedded magnetic cores.

1. INTRODUCTION

Capsule endoscopy (CE) offers significant advantages in noninvasive visualization of gastrointestinal tract and has become a widely adopted diagnostic tool in clinical practice [1–5]. As next-generation CE integrate high-resolution imaging [6], active locomotion [7, 8], and therapeutic functions [9, 10], their power consumption has exceeded 0.5 W. Traditional button batteries cannot support the demand for long-term operation due to capacity limitations. Inductively coupled wireless power transfer (IWPT) enables energy transmission through magnetic coupling between external transmitting coil and internal receiving coil (RC), thereby addressing the power supply bottleneck of CE. The calculation of winding loss in the RC, as the core of accurate evaluation of received power, directly affects the optimal design of the system [11].

Dowell's method is used to calculate the winding resistance in IWPT systems [12]. This method simplifies conductor structures into planar copper foils, establishing a framework for resistance calculation under skin effect and proximity effect. Due to its computational efficiency, it is widely adopted in preliminary design. However, the dual demands of CE miniaturization and higher efficiency necessitate greater accuracy in winding resistance calculations.

In terms of IWPT system optimization, scholars have explored both coil structure design and computational methods [13–15]. Kuang et al. employed Litz wire and achieved magnetic field focusing by optimizing the transmitter coil structure to reduce losses, establishing a mutual power analysis model under a specific configuration [16]. Elizondo et al. systematically compared various high-frequency winding loss models, highlighting that existing analytical models exhibit significant errors in complex core structures such as toroidal inductors, particularly at high frequencies ($>$ 200 kHz) and in multi-layer winding scenarios, where the resistance factor can be overestimated by 93% to 226%. A new analytical model was proposed, which splits the inner and outer windings and incorporates a toroidal factor and equivalent conductivity correction, reducing the deviation to within 20% [17]. Research on the improvement of Dowell's method mainly focuses on introducing compensation coefficients to correct errors resulting from one-dimensional equivalence [18], while two-dimensional (2D) models describe the magnetic field superposition effect of each turn of wire through integral equations, such as using Bessel function expansions to calculate alternating magnetic fields (AMF) [19].

However, existing studies are mainly limited to air-core windings and are lacking in analyzing the influence of magnetic core. To further improve the calculation accuracy of the equivalent series resistance (R_{SR}), this study performs an in-depth comparative analysis of error sources of the two calculation methods within specific winding configuration, and proposes a novel optimization approach. Based on the RC configuration presented in Fig. 1, the research contents are as follows:

1. Analytical models of the RC using Dowell's method and Bessel's method, respectively, which correlate their R_{SR} with design parameters, are built.

* Corresponding author: Jinyang Gao (gjy.1001@163.com).

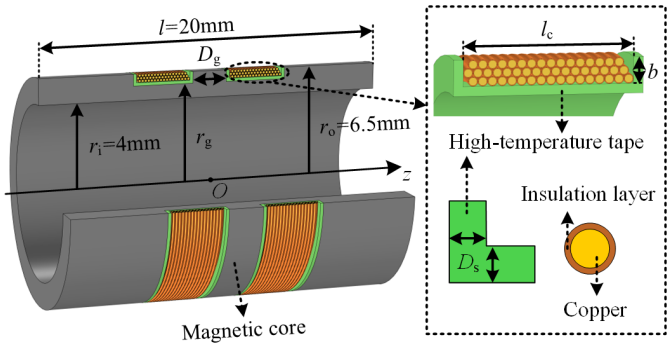

FIGURE 1. Schematic diagram of the receiving coil (RC) configuration.

2. The influence of groove spacing (D_g) and winding layers (N_p) on the R_{SR} is revealed.

3. The prototypes and simulations of RC with identical sizes are fabricated, and their R_{SR} from Dowell's, Bessel's, and the novel Bessel-modified Dowell's (BMD) methods are compared to confirm the superiority of BMD method.

2. THE STRUCTURE OF THE RC

The RC studied herein is fully wound on a dual-groove circular magnetic core, with its key design parameters illustrated in the 3/4 model of the RC as shown in Fig. 1: the total length l = 20 mm, outer diameter r_o = 6.5 mm, and inner diameter r_i = 4 mm are kept unchanged, while N_p and D_g are varied.

The total number of turns N_r is set to 100, with the number of turns per layer given by $N_q = N_r/N_p$. Each sub-winding has an equal number of turns, is connected in series, and is wound in the same direction. The windings on both sides utilize enameled copper wires with thick insulation: bare copper diameter d_0 = 0.15 mm, insulated outer diameter $d \approx 0.18$ mm. This is because the influence of the skin effect on this enameled wire is minimal within the commonly used frequency range of 200–300 kHz, and its resistance is low [20]. The thickness of the high-temperature tape insulation layer D_s = 0.18 mm. The radius of the magnetic core groove r_g, width of the sub-winding l_c, and height of the sub-winding b can be calculated as follows, respectively:

$$r_g = r_o - b - D_s \quad (1)$$

$$l_c = (N_q/2 + 0.5)d \quad (2)$$

$$b = (\sqrt{3}N_p/2 - \sqrt{3}/2 + 1)d \quad (3)$$

3. FINITE ELEMENT ANALYSIS OF RSR

As shown in Fig. 2, 16 different RCs were actually made by changing the structural parameters N_p and D_g, in accordance with the structural parameters defined in Fig. 1. The R_{SR} of each RC was measured using an LCR meter (HIOKI IM3536).

To obtain a reference benchmark for the computed values, a 3D electromagnetic model was established using COMSOL: by discretizing the solution domain into finite elements (referred to as mesh generation), governing equations are formulated and solved, enabling the precise calculation of electromagnetic field

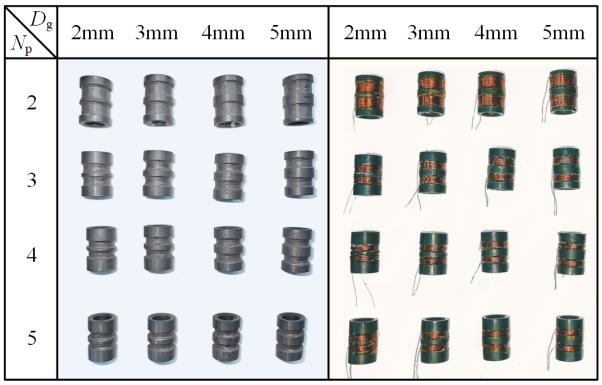

FIGURE 2. The magnetic cores and RCs with different groove spacing (D_g) and winding layers (N_p).

distribution, which is then used to compute R_{SR}. Finite element simulation (FEA) can effectively handle complex geometries, material properties, and boundary conditions, and accurately simulate the electromagnetic field distributions and current flow characteristics of actual windings. Note that, considering the electromagnetic exposure and overheating of RC and their impact on human safety, the frequency was set to 218 kHz [21].

Compare the measured and simulated values of R_{SR}, and a high degree of agreement was found between them, as shown in Fig. 3, which validates the accuracy and reliability of the simulation model.

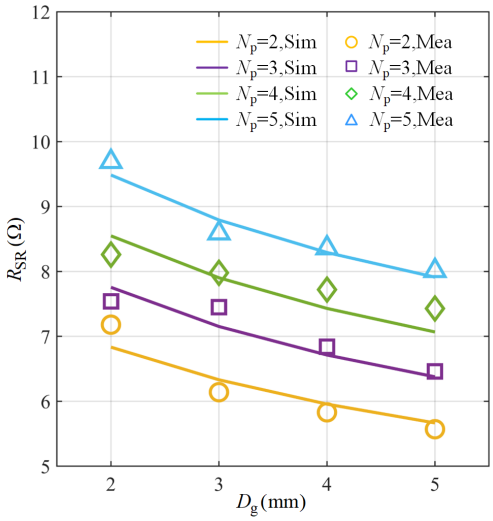

FIGURE 3. Comparison between the measured equivalent series resistance (R_{SR}) and simulated ones.

Considering the unavoidable manufacturing deviations (e.g., dimensional precision) in the manual production process, the simulated R_{SR} values were used as the reference for calculated values in subsequent sections of this paper.

To explore the impact of resistive loss caused by the alternating magnetic field (AMF) for series-connected windings, a simulation study was conducted based on COMSOL. By accurately setting the material parameters and refining the winding region mesh (ensuring that the mesh size was smaller than the

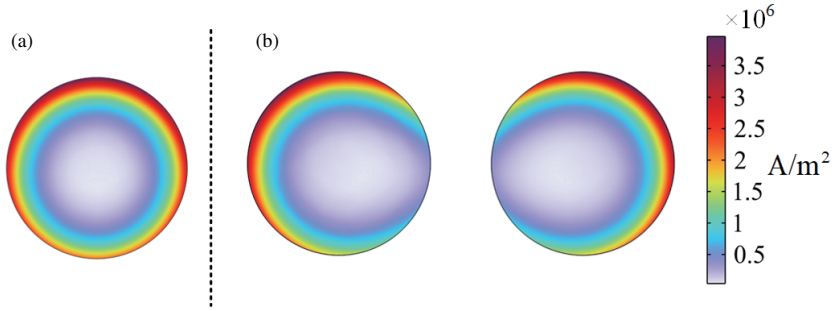

FIGURE 4. Schematic diagram of current density (J) distribution for a circular coil with a radius of 6.41 mm at 218 kHz: (a) Effect of skin effect; (b) Effect of proximity effect.

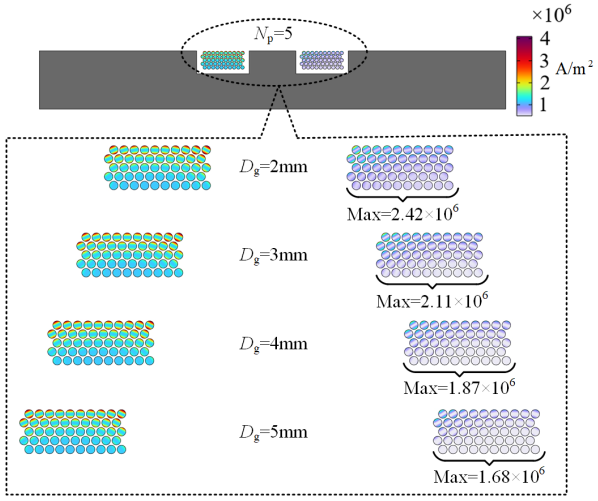

FIGURE 5. Variation of current density (J) with groove spacing D_g (from 2 mm to 5 mm) at N_p = 5.

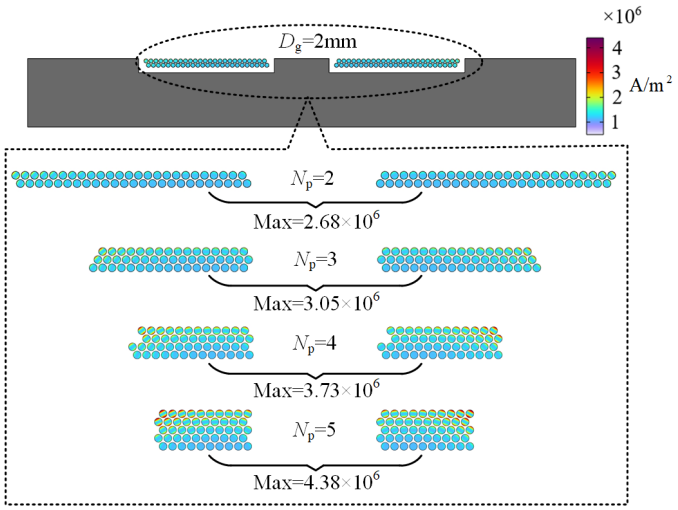

FIGURE 6. Variation of J with winding layers N_p (from 2 to 5 layers) at D_g = 2 mm.

skin depth), we achieved a high-precision capture of the current density J distribution.

J can be calculated as:

$$J = \frac{I}{A_{cu}} \tag{4}$$

where I is the coil current, and $A_{cu} = \pi(d_0 \times 10^{-3}/2)^2$ is the cross-sectional area of the wire. Note that Eq. (4) represents an ideal uniform distribution, whereas Fig. 4 to Fig. 6 illustrate the actual nonuniform J distribution under high-frequency excitation.

As shown in Fig. 4, each annular coil has a radius of 6.41 mm, with a current of 0.02 A, the distance between the two coils is 2 mm. The non-uniformity of the J distribution caused by the skin effect, and the proximity effect at 218 kHz is illustrated in Fig. 4. It can be observed that the skin effect causes the current to concentrate towards the conductor surface, reducing the effective cross-sectional area. This results in increased resistance and generates additional losses. The proximity effect further causes a nonuniform distribution of J within each winding — with J enhanced on the far side and attenuated on the near side — thereby exacerbating resistance losses.

Based on characteristics of the skin effect and proximity effect, two sets of experiments were designed to observe the distribution of J induced by AMF under different D_g and N_p conditions.

To investigate the relationship between J and D_g, a differential excitation experiment was designed, as shown in Fig. 5: N_p was fixed at 5 layers for the RC. An alternating current excitation was applied to the left winding of the dual-winding structure, while the right winding was maintained in an open-circuit state (only generating induced eddy currents). By varying D_g from 2 mm to 5 mm, the change in J within the cross-section of the right winding was observed. The distribution of J in the left winding remains unchanged, while the simulated maximum J values in the right were 2.42×10^6 A/m^2, 2.11×10^6 A/m^2, 1.87×10^6 A/m^2, and 1.68×10^6 A/m^2, respectively, showing a significant decrease with D_g.

To investigate the relationship between J and N_p, D_g was fixed at 2 mm for the RC. As shown in Fig. 6, the two windings were connected in series. By varying N_p from 2 to 5, the variation of J in the cross-sections of both windings was observed. In Fig. 6, the maximum J values for both windings consistently occur on the side facing away from the neighboring conductor, a direct consequence of the proximity effect. The simulated

maximum J values were 2.68×10^6 A/m^2, 3.05×10^6 A/m^2, 3.73×10^6 A/m^2, and 4.38×10^6 A/m^2, respectively, showing a significant increase with N_p.

Higher J values indicate a greater influence of the skin effect and proximity effect, leading to greater winding losses caused by these effects. Fig. 5 and Fig. 6 account for the trend in Fig. 3 that the R_{SR} decreases with D_g and increases with N_p.

4. CALCULATION OF R_{SR}

Figure 7 shows the equivalent circuit diagram of the RC. The RC can be represented by a lumped-parameter model (R_{ac}, L_r, C_{rp}), where R_{ac}, L_r, and C_{rp} represent the AC resistance, inductance, and parasitic capacitance of the RC, respectively. R_{SR} can be calculated as [19]:

$$R_{SR} = \frac{R_{ac}}{\left(1-4\pi^2 f^2 L_r C_{rp}\right)^2 + \left(2\pi f C_{rp} R_{ac}\right)^2} \tag{5}$$

$$R_{ac} = R_{copper} + R_{core} \tag{6}$$

where R_{copper} is the copper loss resistance of the circular coil itself; R_{core} is the magnetic loss resistance of the ferrite core. The calculations for L_r and C_{rp} refer to [22, 23].

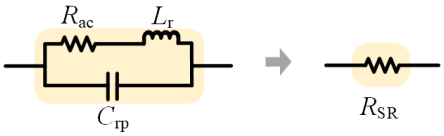

FIGURE 7. Equivalent circuit of the RC.

4.1. Calculation of R_{copper} Using Dowell's Method

As shown in Fig. 8, the core concept of Dowell's method involves simplifying calculations by equating conductors to copper foils. This process consists of two steps: first, a round conductor is converted to a square conductor of equal cross-sectional area. Subsequently, while maintaining constant thickness, the height of the square conductor is adjusted to equal that of the original round conductor.

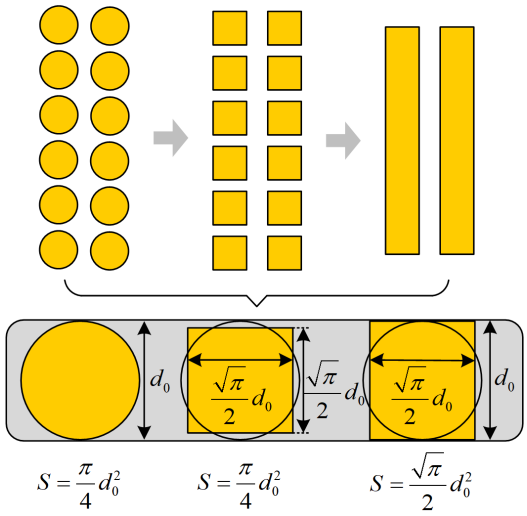

FIGURE 8. Schematic diagram of the equivalence process in Dowell's method (S denotes the cross-sectional area of the conductor).

$R_{\text{copper\_D}}$ can be calculated as:

$$R_{\text{copper\_D}} = R_{dc}(F_s + F_p) \tag{7}$$

where R_{dc} represents the DC resistance; F_s represents the skin effect coefficient; and F_p represents proximity effect coefficient [24], respectively:

$$R_{dc} = \frac{\rho \sum_{i=1}^{N_p} \sum_{j=1}^{N_q} (2\pi r_{ij})}{\pi \left(d_0/2\right)^2} \tag{8}$$

$$F_s = Z \frac{\sinh 2Z + \sin 2Z}{\cosh 2Z - \cos 2Z} \tag{9}$$

$$F_p = Z \frac{2(N_p^2 - 1)}{3} \frac{\sinh Z - \sin Z}{\cosh Z + \cos Z} \tag{10}$$

$$r_{ij} = r_o - \frac{d(\sqrt{3}i - \sqrt{3} + 1)}{2} \tag{11}$$

where $Z = (\pi/4)^{0.75} d_0 \sqrt{\pi f \mu_0 \eta \sigma}$; the permeability of air $\mu_0 = 4\pi \times 10^{-7}$ (H/m); the porosity factor $\eta = \frac{N_p \pi (d_0/2)^2}{db}$, the electrical conductivity $\sigma = 1/\rho$; the resistivity of copper $\rho = 1.75 \times 10^{-8}$ (Ω•m); and r_{ij} is the radius of the j-th turn in the i-th winding layer.

The R_{copper} calculated by Dowell's method is presented in Fig. 9, where it can be observed that:

1. The R_{skin} stabilizes at $3.94 \pm 0.07\,\Omega$. This stability occurs because the N_r of the RC fixed at 100 turns, causing the influence of the skin effect to approach a constant value. Consequently, variations inR_{copper} are primarily influenced by the proximity effect.

2. The R_{copper} increases significantly with N_p but remains unchanged with D_g, thus it cannot reflect the impact of D_g.

This limitation stems from the equivalent process altering the shape of the circular conductor and neglecting the complexity

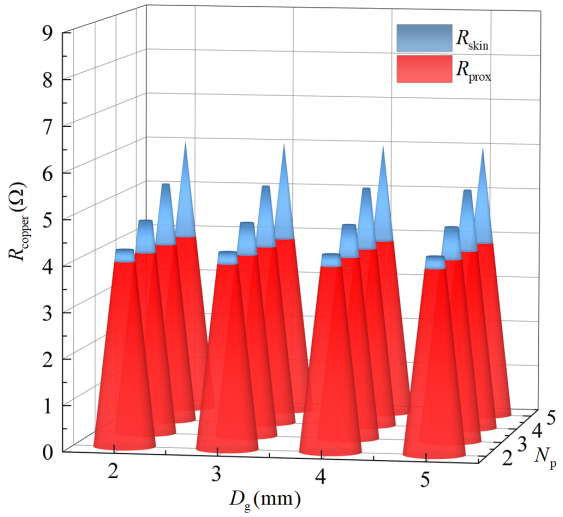

FIGURE 9. Variation of copper loss resistance (R_{copper}) with N_p and D_g busing Dowell's method.

of the winding geometry as well as the effects of interactions between conductors. At high frequencies, this leads to significant calculation errors in proximity effect losses. When $N_p \geq 2$, the proximity effect factor F_p is significantly higher than the skin effect factor F_s [24]. Consequently, Dowell's method yields substantial deviations from actual results when N_p is high.

4.2. Calculation of R_{copper} Using Bessel's Method

The resistance calculation method constructed based on Bessel functions comprehensively considers the winding geometry, interactions between conductors, and the influence of the magnetic field on current flow, enabling accurate calculation of the total winding resistance.

However, the presence of the magnetic core affects the magnetic field distribution around the winding, thereby indirectly influencing the winding resistance. This paper introduces the effective permeability μ_{ij}, namely, the average value of relative permeability of the core to represent this influence, which is calculated as follows:

$$\mu_{ij} = \frac{r_g^2 - r_i^2}{r_{ij}^2}\mu'(z_{ij}) + \frac{r_{ij}^2 - (r_g^2 - r_i^2)}{r_{ij}^2} \tag{12}$$

where z_{ij} is the axial position, and μ' is the ratio of the core inductance to air-core inductance [25].

Figure 10 shows μ' along the axial position z under different structural parameters, with dashed lines indicating maximum values for each N_p. The data indicate that these maximum values increase with N_p significantly and decrease with D_g slightly.

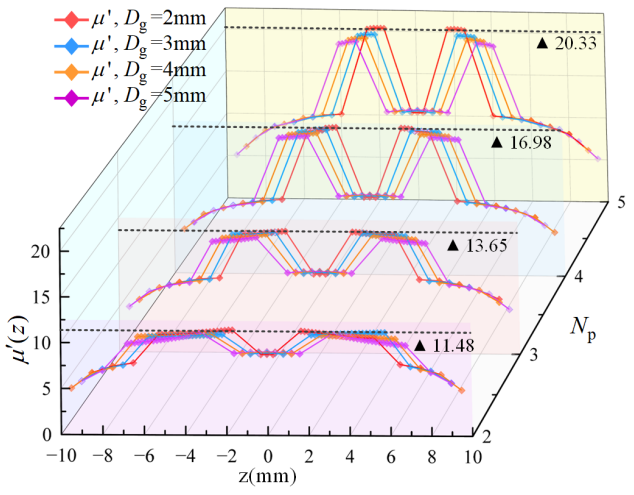

FIGURE 10. Distribution of μ' along axial position z for dual-groove structures with various N_p and D_g.

When alternating current passes through the RC, each turn is affected by AMF generated by both its own current and currents in other turns. This alters the uniformity of current distribution within the turn, leading to power losses. Such power losses are directly related to R_{copper}:

$$R_{\text{copper\_B}} = 2(P_s + P_p)/I^2 \tag{13}$$

where P_s is the power loss caused by the skin effect, and P_p is the power loss caused by the proximity effect. Therefore, accurate calculation of R_{copper} lies in computing these corresponding losses. The detailed calculation method is as follows:

4.2.1. Calculation of P_s

P_s can be calculated as:

$$P_s = \frac{\sum_{i=1}^{N_p}\sum_{j=1}^{N_q} R_{s\_ij} I^2}{2} \tag{14}$$

$$R_{s\_ij} = \frac{2\pi r_{ij} \times 1.05 \times F(\gamma_{ij})}{\sigma\pi(d_0/2)^2} \tag{15}$$

$$F(\gamma_{ij}) = \frac{\gamma_{ij}}{2}\frac{ber(\gamma_{ij})bei'(\gamma_{ij}) - bei(\gamma_{ij})ber'(\gamma_{ij})}{ber'^2(\gamma_{ij}) + bei'^2(\gamma_{ij})} \tag{16}$$

where R_{s_ij} is the skin effect-related resistance of a single-turn coil [19]; 1.05 accounts for the effective length increase due to the helical structure; I is the current passing through the conductor; $\gamma_{ij} = \frac{\sqrt{2}d_0}{2\delta_{ij}}$. The skin depth $\delta_{ij} = \sqrt{\frac{\rho}{\pi f \mu_0 \mu_{ij}}}$.

$ber()$ and $bei()$ are the real and imaginary parts of zeroth-order Kelvin functions, respectively; $ber'()$ and $bei'()$ are the first derivatives of $ber()$ and $bei()$, respectively [26].

4.2.2. Calculation of P_p

P_p can be calculated as:

$$P_p = \sum_{i=1}^{N_p}\sum_{j=1}^{N_q} 2\pi r_{ij} G(\gamma_{ij}) \mid \bar{\mathbf{H}}_{ij} \mid^2 \tag{17}$$

$$G(\gamma_{ij}) = \frac{-2\pi\gamma_{ij}}{\sigma} \cdot \frac{ber_2(\gamma_{ij})ber'(\gamma_{ij}) + bei_2(\gamma_{ij})bei'(\gamma_{ij})}{ber^2(\gamma_{ij}) + bei^2(\gamma_{ij})} \tag{18}$$

$$\bar{\mathbf{H}}_{ij} = \frac{1}{\pi\,(d_0/2)^2}\int_0^{2\pi}\int_0^{d_0/2} \mathbf{H}_{ij}\,(\rho,\varphi)\,\rho d\rho d\varphi \tag{19}$$

$$\mathbf{H}_{ij}(\rho,\varphi) = \sum_{p=1}^{N_p}\sum_{q=1}^{N_q} \mathbf{H}_{pq}(r_{ij} + \rho\sin\varphi, z_{jq} + \rho\cos\varphi)\psi \tag{20}$$

where $G(\gamma_{ij})$ is the conversion function between the AMF and power loss, and $\bar{\mathbf{H}}_{ij}$ is the average external magnetic field strength at the cross-section of the winding in the i-th layer and j-th turn. z_{jq} is the axial distance between the winding in the p-th layer and q-th turn and the winding in the i-th layer and j-th turn. $\psi = 1$ when $p = i$ and $q = j$; otherwise, $\psi = 0$.

In Fig. 11, the center of the winding in the p-th layer and q-th turn is the origin.

$$\mathbf{H}_{pq}(x,z) = \sqrt{\mathbf{H}_x^2(x,z) + \mathbf{H}_z^2(x,z)} \tag{21}$$

$$\mathbf{H}_x(x,z) = \int_0^{2\pi} \frac{r_{pq} I}{4\pi r_Q^3(x,z)} z\cos\theta d\theta \tag{22}$$

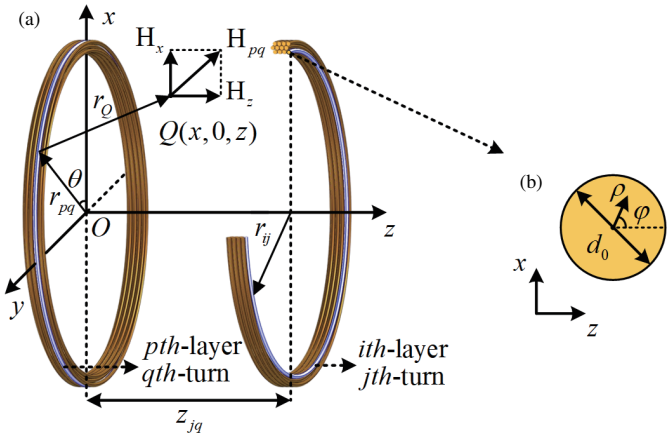

FIGURE 11. (a) Magnetic field schematic for winding at p-th layer and q-th turn; (b) Cross-section of the winding at i-th layer and j-th turn in the xOz plane.

$$\mathbf{H}_z(x,z) = \int_0^{2\pi} \frac{r_{pq} I}{4\pi r_Q^3(x,z)} (r_{pq} - x\cos\theta) d\theta \tag{23}$$

$$r_Q(x,z) = \sqrt{(r_{pq}\cos\theta - x)^2 + (r_{pq}\sin\theta)^2 + (-z)^2} \tag{24}$$

where $\mathbf{H}_{pq}$ is the AMF generated by the winding in the p-th layer and q-th turn; $\mathbf{H}_x$ and $\mathbf{H}_z$ are the components of $\mathbf{H}_{pq}$ in the x-direction and z-direction, respectively; r_Q is the distance from the winding in the p-th layer and q-th turn to the point $Q(x,0,z)$; the calculation of r_{pq} is the same as that of r_{ij} in Eq. (11).

The R_{copper} calculated by the Bessel's method is shown in Fig. 12, where it can be observed that:

1. The R_{skin} stabilizes at $3.16 \pm 0.04\,\Omega$, and the influence of the skin effect becomes constant.

2. The variation of R_{copper} is primarily dominated by the proximity effect, and its value increases with N_p and decreases with D_g.

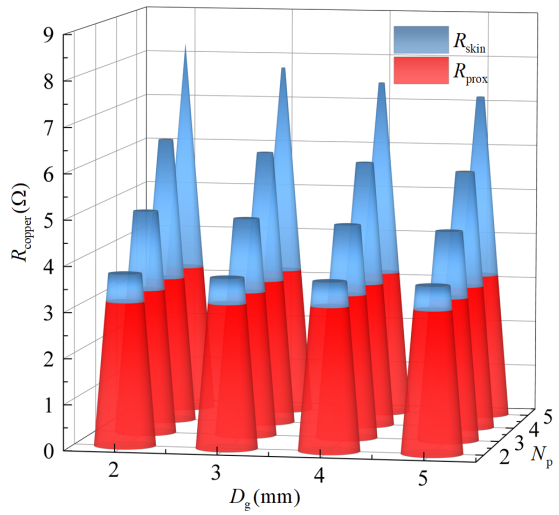

FIGURE 12. Variation of R_{copper} with N_p and D_g using Bessel's method.

4.3. Calculation of R_{core}

R_{core} can be calculated as:

$$R_{core} = \frac{2\pi f L_0 \sum_{i=1}^{N_p} \sum_{j=1}^{N_q} \mu''(z_{ij})}{N_r} \tag{25}$$

where L_0 is the air-core inductance; $f = 218\,\text{kHz}$; and μ'' is the difference between simulated values of the cored resistance and air-core resistance [25].

Figure 13 shows μ'' along the axial position z under different structural parameters, with minima for each N_p marked by dashed lines. The data reveal that these minimum values increase with N_p slightly, while they decrease with D_g slightly.

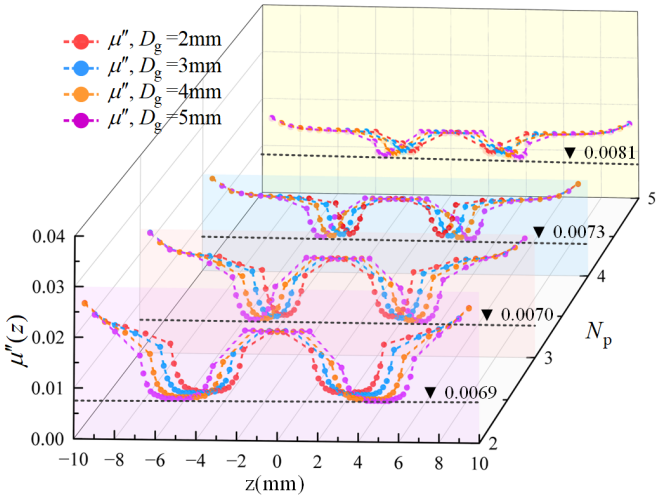

FIGURE 13. Distribution of μ'' along axial position z for dual-groove structures with various N_p and D_g.

By substituting the simulated value of μ'' into Eq. (25), R_{core} is obtained, as shown in Fig. 14. The R_{core} value increases with N_p and decreases with D_g, exhibiting the same variation trend as μ''.

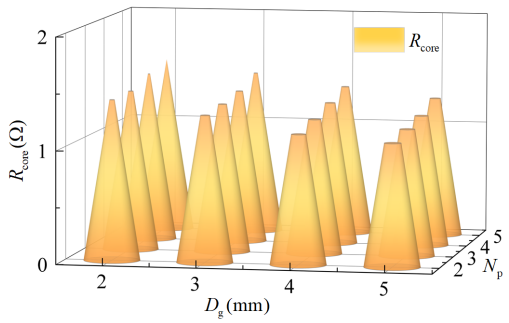

FIGURE 14. Variation of magnetic loss resistance (R_{core}) with N_p and D_g.

5. ERROR ANALYSIS

In the overall accuracy assessment, the Root Mean Squared Error (RMSE) comprehensively reflects the accuracy of both the calculation methods. The RMSE values between calculated R_{SR} values and simulated ones are 1.0131 for Bessel's method

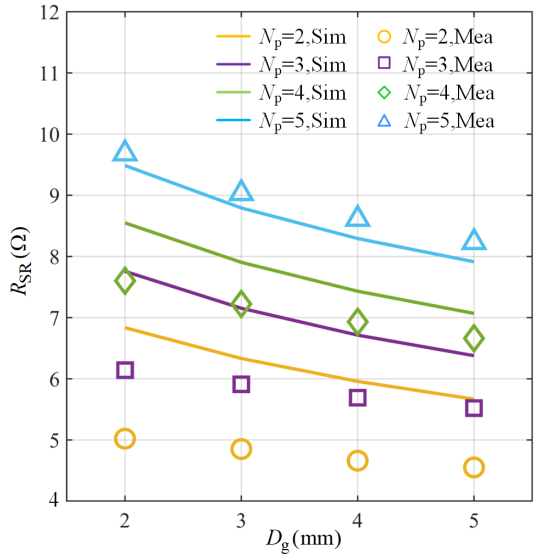

FIGURE 15. Comparison between the calculated R_{SR} using Bessel's method and simulated ones.

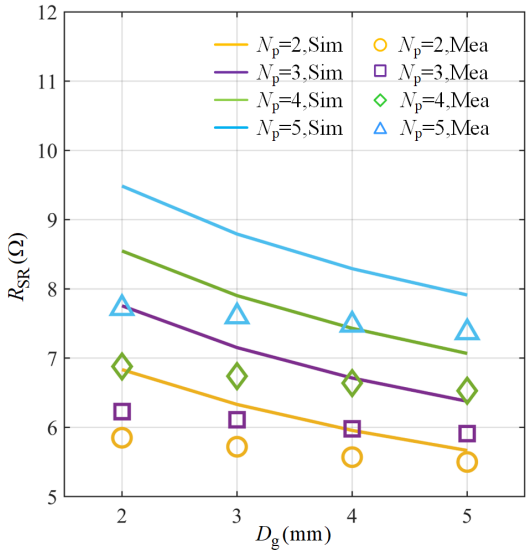

FIGURE 16. Comparison between the calculated R_{SR} using Dowell's method and simulated ones.

and 1.0070 for Dowell's method, respectively. The difference in accuracy between the two methods is less than 1%, indicating that their overall error levels are similar across the entire dataset.

As showed in Figs. 15 and 16, both Bessel's method and Dowell's method calculations of R_{SR} exhibit an underestimation trend compared to the simulated values, with neither method providing an adequate fit to simulation values. To further optimize calculated results, the analysis is conducted in terms of N_p and D_g, combined with the geometric structure of the RC.

In Fig. 17, deviation is defined as the difference between calculated and simulated values, with bar charts indicating the mean deviation. It can be found that:

1. Bessel's method demonstrates higher accuracy when $D_g \leq 4$ mm, and deviations decrease with N_p. As shown in Fig. 15, the calculated and simulated values show good agreement at $N_p = 5$.
2. Dowell's method achieves higher accuracy when $D_g > 4$ mm, and deviations increase with N_p. As shown in Fig. 16, the closest match to simulated values occurs in simplified structures with $N_p = 2$ and $D_g = 5$ mm.

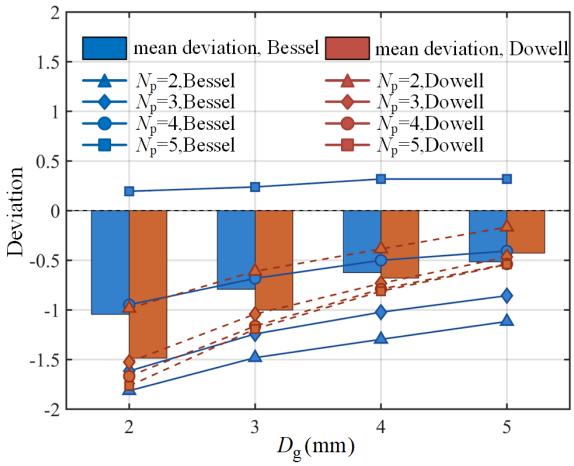

FIGURE 17. Change of calculation deviations with N_p and D_g when using the Bessel's and Dowell's methods (Bar height represents mean deviation).

The accuracy of the two methods varies significantly with changes in the RC structural parameters N_p and D_g. Building on the previous analysis, an improved method was proposed to optimize computational efficiency.

6. BESSEL-MODIFIED DOWELL'S (BMD) METHOD

The conventional Dowell's method simplifies the winding into planar conductor layer for calculation, which exhibits a significant limitation: when D_g varies, the proximity effect loss calculated remains constant, as showed in Fig. 9, leading to excessive deviation in the calculation of R_{SR}.

To address this limitation of Dowell's method, we propose a novel Bessel-modified Dowell's (BMD) method by integrating the framework of Dowell's method with a proximity-effect correction term from Bessel's method. The $R_{\text{copper\_BMD}}$ value using the BMD method can be calculated as:

$$R_{\text{copper\_BMD}}(D_g, N_p) = R_{\text{copper\_D}}(D_g, N_p) + \Delta \quad (26)$$

$$\Delta = R_{\text{copper\_B}}(D_g, N_p) - R_{\text{copper\_B}}(D_g = 5\,\text{mm}, N_p) \quad (27)$$

where $R_{\text{copper\_D}}$ is the R_{copper} calculated using Dowell's method in Eq. (7); $R_{\text{copper\_B}}$ is the R_{copper} calculated using Bessel's method in Eq. (13); Δ represents the increment of R_{copper} caused by proximity effects under different D_g. Substitute Eq. (26) into Eqs. (5) and (6) to calculate R_{SR} values of the BMD method.

The method addresses the limitations of traditional Dowell's method by incorporating the increment of R_{copper} caused by the proximity effect into $R_{\text{copper\_D}}$ when D_g changes.

The result in Fig. 18 shows that BMD method achieves significant improvement over Dowell's method presented in Fig. 16.

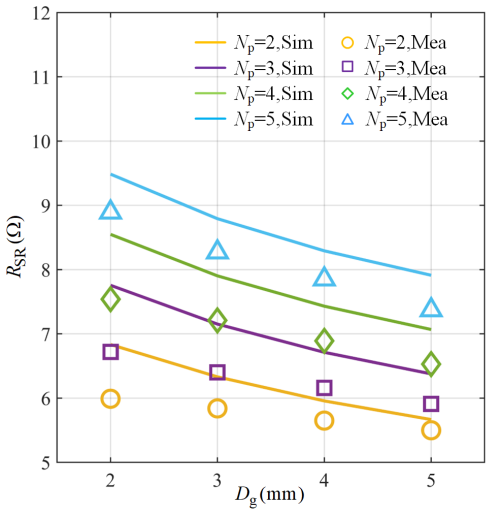

FIGURE 18. Comparison between the calculated R_{SR} using Bessel-modified Dowell's (BMD) method and simulated ones.

The relative error is the absolute value of the ratio of the deviation to simulation value, multiplied by 100%, which provides a more intuitive understanding of the degree to which the calculated values deviate from the simulation values. As shown in Fig. 19, Dowell's method exhibits relative errors ranging from 2.97% to 19.72%, with a mean value of 11.71%. Bessel's method exhibits relative errors ranging from 2.09% to 26.52%, with a mean value of 12.69%. After the correction, the relative errors were reduced to a range of 2.97% to 13.40%, with a mean value of 7.99%, showing significant improvement compared to the uncorrected Dowell's method. The red line and red dot represent the median and mean, respectively. The closeness of these two values indicates a symmetric error distribution, which demonstrates the high reliability of the BMD method.

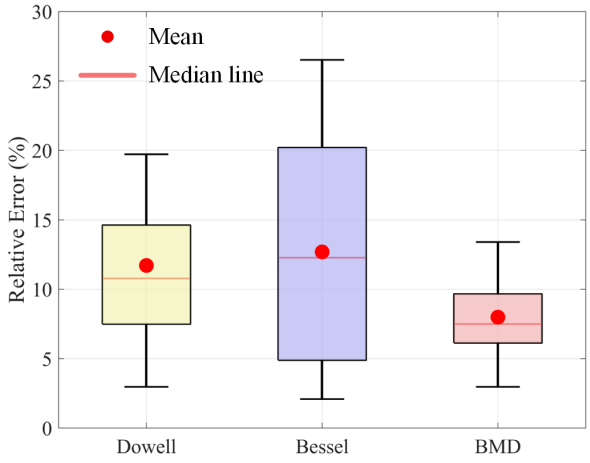

FIGURE 19. Comparison of statistical characteristics for relative errors of three calculation methods.

7. CONCLUSION

This study establishes an accurate calculation model for the R_{SR} of the receiving coil (RC). Under fixed overall dimensions and turn count, variations in the winding layer (N_p) and groove spacing (D_g) reveal that equivalent series resistance (R_{SR}) fluctuations are primarily driven by the proximity effect losses. The Dowell's method, due to its equivalent hypothesis, cannot reflect the impact of changes in D_g on proximity effect loss, resulting in significant errors when $D_g \leq 4$ mm. By introducing the average of relative permeability (μ_{ij}) to analyze the magnetic field, Bessel's method investigates the influence of proximity losses with varying N_p and D_g. However, both methods exhibit a systematic underestimation compared to simulated values. To address this, this paper proposes a Bessel-corrected Dowell's (BMD) method that reduces the maximum relative error from 19.72% (mean 11.71%) to below 13.40% (mean 7.99%). This method provides an effective tool for the rapid design optimization of magnetic-core-embedded annular coils.

ACKNOWLEDGEMENT

This work was supported by the National Natural Science Foundation of China (Grant No. 52275038 and No. 61803347), the Shanxi Province Science Foundation for Excellent Youth (Grant No. 202203021224007), the Special Program of China Postdoctoral Science Foundation (Grant No. 2025T180991), and the General Program of China Postdoctoral Science Foundation (Grant No. 2024M763026).

REFERENCES

[1] Flemming, J. and S. Cameron, "Small bowel capsule endoscopy indications, results, and clinical benefit in a university environment," *Medicine*, Vol. 97, No. 14, e0148, Apr. 2018.

[2] Youssef, F. F., L. L. Branch, M. Kowalczyk, and T. J. Savides, "Endoscopic approaches for managing small intestinal disease," *Annual Review of Medicine*, Vol. 76, 155–165, Jan. 2025.

[3] Zhao, K., Y. F. Yang, and J. P. Wang, "Clinical value of capsule endoscopy in small intestinal diseases," *Zhonghua Nei Ke Za Zhi*, Vol. 59, No. 2, 124–128, 2020.

[4] Cao, Q., R. Deng, Y. Pan, R. Liu, Y. Chen, G. Gong, J. Zou, H. Yang, and D. Han, "Robotic wireless capsule endoscopy: Recent advances and upcoming technologies," *Nature Communications*, Vol. 15, No. 1, 4597, May 2024.

[5] Khan, S. R., S. K. Pavuluri, G. Cummins, and M. P. Y. Desmulliez, "Wireless power transfer techniques for implantable medical devices: A review," *Sensors*, Vol. 20, No. 12, 3487, Jun. 2020.

[6] Jiang, B., Y.-Y. Qian, J. Pan, X. Jiang, Y.-C. Wang, J.-H. Zhu, W.-B. Zou, W. Zhou, Z.-S. Li, and Z. Liao, "Second-generation magnetically controlled capsule gastroscopy with improved image resolution and frame rate: A randomized controlled clinical trial (with video)," *Gastrointestinal Endoscopy*, Vol. 91, No. 6, 1379–1387, 2020.

[7] Gao, J., G. Yan, Z. Wang, S. He, F. Xu, P. Jiang, and D. Liu, "Design and testing of a motor-based capsule robot powered by wireless power transmission," *IEEE/ASME Transactions on Mechatronics*, Vol. 21, No. 2, 683–693, Apr. 2016.

[8] Khodaee, Z., M. R. Zakerzadeh, and M. G. S. Damghanizadeh, "Enhancing capsule endoscopy with an orient-controllable internal actuation mechanism: Proof of concept," *Mechatronics*, Vol. 106, 103296, Apr. 2025.

[9] Song, Z., W. Zhang, W. Zhang, and D. Paolo, "A novel biopsy capsule robot based on high-speed cutting tissue," *Cyborg and Bionic Systems*, Vol. 2022, Article ID 9783517, 2022.

[10] Sidhu, M., N. Shahidi, S. Gupta, L. Desomer, S. Vosko, W. A. v. Hattem, L. F. Hourigan, E. Y. T. Lee, A. Moss, S. Raftopoulos, S. J. Heitman, S. J. Williams, S. Zanati, D. J. Tate, N. Burgess, and M. J. Bourke, "Outcomes of thermal ablation of the mucosal defect margin after endoscopic mucosal resection: A prospective, international, multicenter trial of 1000 large nonpedunculated colorectal polyps," *Gastroenterology*, Vol. 161, No. 1, 163–170, Jul. 2021.

[11] Cui, C., Q. Zhao, and Z. Li, "Design of wireless power supply optimized structure for capsule endoscopes," *Journal of Power Technologies*, Vol. 96, No. 2, 101–109, 2016.

[12] Dowell, P. L., "Effects of eddy currents in transformer windings," in *Proceedings of the Institution of Electrical Engineers*, Vol. 113, No. 8, 1387–1394, 1966.

[13] Han, D., R. Wen, G. Yan, D. Qian, S. Kuang, P. Jiang, and Z. Wang, "Stable wireless power transfer system for capsule robot using three-dimensional hybrid transmitting coil pairs," *IEEE Transactions on Power Electronics*, Vol. 40, No. 6, 8824–8833, Jun. 2025.

[14] Hua, D., L. Deng, J. Gołdasz, X. Liu, H. Du, G. Królczyk, W. Li, and Z. Li, "Functional capsule robots: A review of locomotion, pose, medical operation and wireless power transmission reported in 2018-2023," *Smart Materials and Structures*, Vol. 33, No. 7, 073002, 2024.

[15] Gao, J., J. Zhou, C. Yuan, Z. Zhang, C. Gao, G. Yan, R. Li, and L. Zhang, "Stable wireless power transmission for a capsule robot with randomly changing attitude," *IEEE Transactions on Power Electronics*, Vol. 38, No. 2, 2782–2796, Feb. 2023.

[16] Kuang, S., G. Yan, and Z. Wang, "Optimization design for receiving coil with novel structure based on mutual coupling model in wireless power transmission for capsule endoscope," *Energies*, Vol. 13, No. 23, 6460, Jul. 2020.

[17] Elizondo, D., E. L. Barrios, A. Ursúa, and P. Sanchis, "Analytical modeling of high-frequency winding loss in round-wire toroidal inductors," *IEEE Transactions on Industrial Electronics*, Vol. 70, No. 6, 5581–5591, Jun. 2023.

[18] Kutkut, N. H., "A simple technique to evaluate winding losses including two-dimensional edge effects," *IEEE Transactions on Power Electronics*, Vol. 13, No. 5, 950–958, 1998.

[19] Gao, J., S. Tian, C. Yuan, Z. Ma, C. Gao, G. Yan, R. Li, Q. Tan, and L. Zhang, "Design and optimization of a novel double-layer Helmholtz coil for wirelessly powering a capsule robot," *IEEE Transactions on Power Electronics*, Vol. 39, No. 1, 1826–1839, Jan. 2024.

[20] Gao, J. and G. Yan, "Design and implementation of a clamper-based and motor-driven capsule robot powered by wireless power transmission," *IEEE Access*, Vol. 7, 138 151–138 161, Sep. 2019.

[21] Jia, Z. W., G. Yan, Jiangpingping, W. Zhiwu, and L. Hua, "Efficiency optimization of wireless power transmission systems for active capsule endoscopes," *Physiological Measurement*, Vol. 32, 1561–1573, Aug. 2011. [Online]. Available: https://api.semanticscholar.org/CorpusID:24911432

[22] RamRakhyani, A. K., S. Mirabbasi, and M. Chiao, "Design and optimization of resonance-based efficient wireless power delivery systems for biomedical implants," *IEEE Transactions on Biomedical Circuits and Systems*, Vol. 5, No. 1, 48–63, Feb. 2011.

[23] Yang, Z., W. Liu, and E. Basham, "Inductor modeling in wireless links for implantable electronics," *IEEE Transactions on Magnetics*, Vol. 43, No. 10, 3851–3860, Oct. 2007.

[24] Kazimierczuk, M., *High-Frequency Magnetic Components*, John Wiley & Sons, 2009.

[25] Gao, J., *et al.*, "Optimization of a powering coil onboard a dime-size inchworm-like robot for exploring the intestine," *Journal of Shanghai Jiaotong University*, Vol. 54, 152–159, Oct. 2020.

[26] Abramowitz, M. and I. A. Stegun, *Handbook of Mathematical Functions: with Formulas, Graphs, and Mathematical Tables*, National Bureau of Standards, 2006.